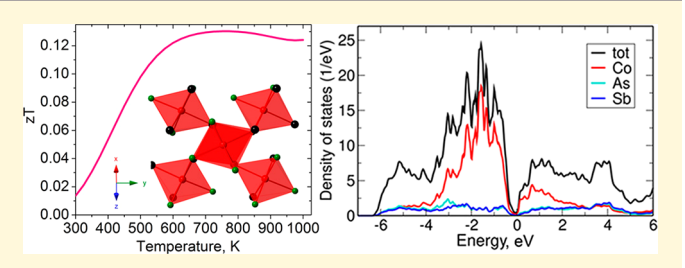


Thermoelectric Properties of CoAsSb: An Experimental and Theoretical Study

Xiaoyan Tan, [†] Kasey P. Deylin, [§] Xiaoyu Deng, [‡] Chang-Jong Kang, [‡] Mark Croft, [‡] Corey E. Frank, [†] Chongin Pak, Saul Lapidus, Susan M. Kauzlarich, Valentin Taufour, Gabriel Kotliar, ** and Martha Greenblatt*,†®

Supporting Information

ABSTRACT: Polycrystalline samples of CoAsSb were prepared by annealing a stoichiometric mixture of the elements at 1073 K for 2 weeks. Synchrotron powder X-ray diffraction refinement indicated that CoAsSb adopts arsenopyrite-type structure with space group $P2_1/c$. Sb vacancies were observed by both elemental and structural analysis, which indicate CoAsSb_{0.883} composition. CoAsSb was thermally stable up to 1073 K without structure change but decomposed at 1168 K. Thermoelectric properties were measured from 300 to 1000 K



on a dense pellet. Electrical resistivity measurements revealed that CoAsSb is a narrow-band-gap semiconductor. The negative Seebeck coefficient indicated that CoAsSb is an n-type semiconductor, with the maximum value of $-132 \mu V/K$ at 450 K. The overall thermal conductivity is between 2.9 and 6.0 W/(m K) in the temperature range 300-1000 K, and the maximum value of figure of merit, zT, reaches 0.13 at 750 K. First-principles calculations of the electrical resistivity and Seebeck coefficient confirmed n-type semiconductivity, with a calculated maximum Seebeck coefficient of $-87 \mu V/K$ between 900 and 1000 K. The difference between experimental and calculated Seebeck coefficient was attributed to the Sb vacancies in the structure. The calculated electronic thermal conductivity is close to the experimental total thermal conductivity, and the estimated theoretical zT based solely on electronic thermal conductivity agrees with experimental values in the high temperature range, above 800 K. The effects of Sb vacancies on the electronic and transport properties are discussed.

■ INTRODUCTION

Thermoelectric materials are of current interest due to the green applications of the conversion of waste heat into usable energy. Presently, almost 200 years after the initial discoveries of the Seebeck and Peltier effects, scientists are still discovering and improving thermoelectric materials. The performance of a thermoelectric material is characterized by the dimensionless figure of merit, $zT = S^2 \sigma T / \kappa$, where S is the Seebeck coefficient, σ is the electrical conductivity, and κ is the thermal conductivity. Only a relatively few thermoelectric materials have been well studied, and there are a large number of relevant semiconductor phases for which S and κ have not been measured; hence, the discovery of new structure types and compounds with substantial zT is promising. Computational predictions are becoming powerful tools in the discovery and design of new thermoelectric materials, even though it is still challenging to accurately predict thermoelectric properties. 1-3 In recent years, machine learning has also emerged as a useful technique to find possible thermoelectric materials, using databases of experimental results and/or first-principles calculations.4-6 Therefore, it is

essential to develop this important area with new materials that are thoroughly studied by both theoretical and experimental techniques.

Transition metal pnictides are a rich class of thermoelectric materials.⁷⁻¹¹ A recent interesting example is the semiconductor FeSb2, which has received extensive attention due to its anomalously giant S of $-45\,000~\mu\text{V}~\text{K}^{-1}$ at 10 K and other exotic properties, which are still not fully understood. 12-20 FeSb₂ crystallizes in the mineral marcasite-type (FeS₂) structure with a narrow band gap (0.1–0.3 eV) and a power factor (PF = $S^2\sigma$) larger than 2000 μ W K⁻² cm^{-1,21-23} However, due to the large κ , its zT is very small (0.005 at 12 K). The thermoelectric properties of FeSb₂ have been improved, but only to a small degree via substitutions of other elements on the Fe or Sb site.² Considering that $FeAs_2$ is of the same structure type and shows a similarly large PF, ¹⁴ we set out to substitute half of the Sb in

Received: December 15, 2017 Revised: June 6, 2018 Published: June 7, 2018



Department of Chemistry and Chemical Biology and Department of Physics and Astronomy, Rutgers, The State University of New Jersey, Piscataway, New Jersey 08854, United States

[§]Department of Chemistry and [∥]Department of Physics, University of California, Davis, Davis, California 95616, United States

 $^{^{\}perp}$ Department of Chemistry and Biochemistry, Florida State University, Tallahassee, Florida 32306, United States

^{*}Advanced Photon Source, Argonne National Laboratory, Argonne, Illinois 60439, United States

FeSb₂ with As to lower κ and improve zT by minimizing the phonon contributions. However, numerous efforts to synthesize FeAsSb by both solid state and chemical vapor transport reactions have failed to yield the targeted phase. Because of the similarity of the crystallographic and electronic structure of FeSb₂ and CoPn₂ (Pn = As, Sb), investigations were directed to CoAsSb.

CoPn₂ have been reported with arsenopyrite-type (FeAsS) structure, which is very similar to marcasite type (Figure 1).^{32,33}

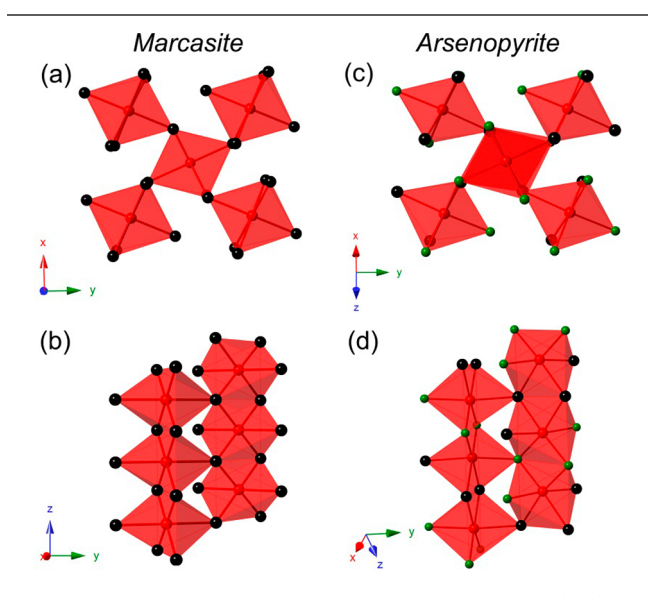


Figure 1. Crystal structures of CoAsSb with marcasite-type (a, b) and arsenopyrite-type structures (c, d). Color code: Co = red and As/Sb = black in (a, b); Co = red, As = black, and Sb = green in (c, d).

Like FeSb₂, CoPn₂ are small-band-gap semiconductors.³⁴ At high temperature, both CoAs₂ (800 K) and CoSb₂ (644 K) convert to marcasite.^{35,36} The thermal transport properties have been reported with larger zT values (~0.1) than that of FeSb₂.³⁴ With possible lower κ , CoAsSb was expected to exhibit better thermoelectric properties compared to CoPn₂. Moreover, Siegrist and Hulliger mentioned CoAsSb with a $S = -180~\mu V~K^{-1}$ in their study of CoPn₂ (Pn = As, Sb) at high temperature.³⁶ CoAsSb was later discovered in nature as the mineral oenite, but there was no detailed study of its synthesis, structure, or thermoelectric properties.³⁷

In this article, we report that arsenopyrite-type CoAsSb can be synthesized by conventional solid state techniques. The structural, magnetic, and thermoelectric properties above and below room temperature have been investigated. Comparison of the results of the experiments and first-principles calculations of the electronic and thermoelectric properties of CoAsSb is also reported.

■ MATERIALS AND METHODS

Starting Materials and Synthesis. The target phase was prepared by conventional solid state methods with cobalt (99.5 wt %, Alfa Aesar), arsenic (99.99 wt %, Alfa Aesar), and antimony powders (99.999 wt %, Alfa Aesar). Elements were mixed in the ratio of Co:As:Sb = 1:1:1, ground thoroughly, and pressed into a pellet. The pellet was loaded into an alumina crucible inside a silica tube which was sealed under vacuum ($<10^{-2}$ mbar). The ampule was heated in a furnace at 1073 K for 2 weeks and then cooled over the course of 6 h. All sample preparations were carried out in an Ar-filled glovebox with O_2 and O_3 and O_4 concentration below 1 ppm.

Laboratory and Synchrotron Powder X-ray Diffraction (PXD and SPXD). Samples were measured in the 2θ range from 10° to 80°

and collected for 1 h on a Bruker D8 Advance diffractometer (Cu K α , $\lambda=1.5418$ Å) with a SOL-X solid state detector. Room temperature SPXD ($\lambda=0.414\,532$ Å) was collected in the 2θ range from 0.5° to 50° at the 11-BM beamline at the Advanced Photon Source (APS) of Argonne National Laboratory. Rietveld refinement of the collected data was carried out with the FullProf package. ³⁸

Magnetic Measurements. Magnetic properties were measured on a polycrystalline sample with a Quantum Design SQUID MPMS-XL magnetometer. Field-cooled (FC) and zero-field-cooled (ZFC) magnetizations were measured between 1.8 and 300 K in a direct-current applied field of 0.5 T. Field dependence of magnetization measurements was performed at 1.8 K with the applied field varying from 0 to 7 T.

Consolidation of Powder. A Dr. Sinter Lab Jr. SPS-211Lx spark plasma sintering (SPS) system (Sumitomo, Tokyo, Japan) was used to consolidate the bulk powder sample (about 1.4 g) into a dense pellet in a 12.7 mm high-density graphite die (POCO) under vacuum (<10 Pa). The temperature was increased from room temperature to 700 °C in 4 min. Once the temperature reached 700 °C, the force loaded increased from 3 kN to approximately 8 kN. After 10 min of dwelling at 700 °C, the pressure was released, and the depressurized samples were cooled to room temperature. The geometrical sample density was larger than 91% of the theoretical density.

Thermogravimetric Analysis (TGA) and Differential Scanning Calorimetry (DSC). A powder sample of about 30 mg was loaded into an alumina crucible in an SDT Q600 TA Instruments and measured between room temperature and 1000 °C at a heating and cooling rate of 10 °C/min under argon flow. The remaining powder after the measurement was analyzed by PXD.

Thermal Conductivity. Thermal diffusivity (D) data were collected from 300 to 1000 K on a dense pellet obtained from SPS with a Netzsch LFA-457 laser flash apparatus. The pellet surface was polished and coated with graphite. The measurement was conducted under dynamic argon atmosphere with a flow rate of 50 mL/min. Thermal conductivity was calculated with the equation $\kappa_{\text{total}} = D \times \rho \times C_p$, where ρ is the density and C_p is the heat capacity. Room-temperature density was measured by the geometric method. The C_p was estimated from the Dulong–Petit law.

Seebeck Coefficient and Electrical Resistivity. A Linseis LSR-3 unit was employed to measure $S_{\rm exp}$ and $\rho_{\rm exp}$ via a four-probe method from 325 to 1000 K under a helium atmosphere on a barshaped sample. The sample, the thermal diffusivity of which was previously measured, was cut into a 12 mm bar using a Buehler diamond saw and polished into a $2.24 \times 1.25 \times 12.62 \ {\rm mm}^3$ bar before measurement. The probe distance was 8 mm, and a thermal gradient of 50 K was applied. $S_{\rm exp'}$ $\rho_{\rm exp'}$ and $\kappa_{\rm total}$ vs temperature data were fit to sixth-order polynomial functions to calculate zT values.

Transport Properties below Room Temperature. The low-temperature transport properties were measured on a 2 \times 2 mm square, cut from a consolidated 12.7 mm pellet (\geq 91% dense), from 10 to 400 K with the commercial multipurpose Physical Properties Measurement System (PPMS, Quantum Design). The $S_{\rm exp}$ and $\kappa_{\rm total}$ were measured with the thermal transport option.

Hall Measurements. The room-temperature Hall coefficient was measured in a Quantum Design physical property measurement system (PPMS) with a four-probe ac method. The Hall coefficient was extracted from the difference between positive and negative field between 9 and -9 T. Platinum leads (0.002 in.) were connected to the bar with silver paste (Wellie-Store). Carrier concentration was calculated by the equation $R_{\rm H}=-1/ne$ using the average of $R_{\rm H}$ from the maximum positive and negative magnetic fields.

Chemical Analysis. Elemental analyses of the prepared samples were performed with a Zeiss Sigma field emission scanning electron microscope (SEM) with Oxford energy dispersive X-ray spectroscopy (EDX).

Theoretical Calculations. First-principles calculations based on density functional theory (DFT) were performed for CoAsSb with the full-potential linearized augmented plane wave method as implemented in the WIEN2k package.³⁵ The muffin tin radii were chosen to be the 2.26, 2.15, and 2.35 Bohr radii for Co, As, and Sb, respectively, and

the cutoff parameter $R_{\rm mt}K_{\rm max}$ was 7.0. The transport properties including $S_{\rm calc}$, $\rho_{\rm calc}$ and $\kappa_{\rm elec}$ were computed with the BoltzTrap package. ⁴⁰ Local density approximations (LDA) were used for the exchange-correlation functional. The semiclassical Boltzmann theory as implemented in the transport code BoltzTrap was used to compute the transport coefficients with a dense $47 \times 43 \times 47$ k-mesh of the entire Brillouin zone. Convergence test for the k-mesh confirmed that the dense $47 \times 43 \times 47$ k-mesh is sufficient to calculate the transport coefficients. DFT relaxation was also performed based on the experimental structure. The resultant lattice parameters are a = 6.22918, b = 6.14171, c = 6.26213 Å, and $\beta = 116.17^{\circ}$. The modified Becke–Johnson (mBJ) exchange potential method was utilized in the DFT relaxed structure to estimate the band gap more precisely. The other computational parameters used in the mBJ method are the same as in the local density approximations. ⁴¹

■ RESULTS AND DISCUSSION

Crystal Structure and Thermal Stability. Similar to the synthesis of CoPn₂ (Pn = As, Sb), CoAsSb was prepared by conventional solid-state methods. The PXD pattern of CoAsSb is similar to those of CoPn₂, but shifts according to unit cell change. Because CoPn₂ adopt arsenopyrite-type structure at room temperature, but undergo transition to marcasite-type structure at higher temperature, ^{35,36} CoAsSb was expected to exhibit either marcasite or arsenopyrite-type structure. These two structure types are closely related as shown in Figure 1.

In the marcasite-type structure (space group Pnnm), $CoPn_6$ octahedra share corners in the orthorhombic ab-plane, with equal in-plane Co-Pn bond distances, which is distinct from the two equal Co-Pn bond distances perpendicular to the plane. Thus, each $CoPn_6$ octahedron is distorted. $CoPn_6$ octahedra form linear chains via edge-sharing along the orthorhombic c-axis. In the Pnnm space group, Co occupies the special position (0, 0, 0), while As and Sb atoms are disordered on the same site (x, y, 0). In the arsenopyrite-type monoclinic structure (space group $P2_1/c$), the three-dimensional (3D) arrangement of $CoPn_6$ octahedra is the same as in marcasite, but with ordered As and Sb. In arsenopyrite, Co, Co, Co, and Co each occupies different general sites at (x, y, z) of $CoPn_6$ octahedra are distorted differently than in marcasite, with six different Co-Pn bond distances.

In the PXD pattern of arsenopyrite a few extra weak peaks are expected relative to those of marcasite structure due to its lower symmetry (Figure S1). Rietveld refinement of the SPXD pattern indicated that the data is best fit with arsenopyrite-type structure (Figure 2).

The indices $(\overline{1}11)$ and $(\overline{1}02)$ are forbidden in marcasite *Pnnm*. Data analysis also indicates about 2.58(3) % CoAs as impurity in the sample. The refined unit cell parameters of CoAsSb are a = 6.23704(6), b = 6.13276(4), c = 6.21963(6) Å, and V =212.648(3) Å³, which are in reasonable agreement with those of CoAs₂ (a = 5.9106(5), b = 5.8680(6), c = 5.9587(5) Å, and V = 185.06(3)) and CoSb₂ (a = 6.5077(3), b = 6.3879(4), c =6.5430(3) Å, and V = 240.91(2). Refinement of each atom site reveals that the Sb site occupancy is 0.883(1), which leads to the chemical composition of CoAsSb_{0.883}. The Sb site can also be refined as a mixed Sb/As position (0.7Sb/0.3As) with full occupancy; however, this model is contradicted by the EDX results. The CoPn₆ octahedron is distorted with Co-As distances of 2.377(1), 2.347(2), and 2.389(2) Å and Co-Sb distances of 2.528(2), 2.531(2), and 2.575(1) Å. The angles of As-Co-As (90.8°, 95.6°, and 106.3°) and Sb-Co-Sb (84.8°, 87.8°, and 86.9°) are not equal to 90°. Other refined parameters for both phases are given in Table S1.

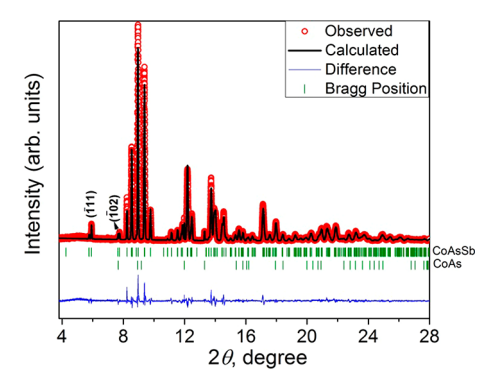


Figure 2. Rietveld refinement of synchrotron powder X-ray diffraction pattern of CoAsSb (space group $P2_1/c$) with wavelength $\lambda = 0.414\,532$ Å. Red circles are the observed pattern, black line is the calculated pattern, vertical green bars are the Bragg positions expected for CoAsSb and CoAs, and the blue line is the difference between observed and calculated patterns.

The CoAsSb composition was also determined by EDX microanalysis of powder particles of mainly $\sim 100~\mu m$ on a scanning electron microscope (Figure S2). In each particle, Co, As, and Sb elements are homogeneously distributed (Figure 3), with the molar ratio of Co:As:Sb close to 1:0.97:0.87, in agreement with results obtained from Rietveld refinement. For the sake of simplicity, the composition ratio of 1:1:1 will be assumed in the discussions that follow.

The stability of the CoAsSb phase was determined by thermogravimetric analysis (TGA) and differential scanning calorimetry (DSC) between room temperature and 1273 K under argon flow. CoAsSb is thermally stable below 1073 K without any phase transition or melting (Figure 4); however, the sample mass drops as the temperature increases from 1073 to 1273 K. The endothermal peak shown in the DSC curve at 1168 K indicates decomposition. The PXD pattern of the sample after TGA-DSC experiment was identified as CoAs_{0.5}Sb_{0.5} (Figure S3). This behavior is different from those of CoAs₂ and CoSb₂, which display a structural transition at 800 and 644 K, respectively.

Magnetic Properties. Magnetic measurements of the CoAsSb powder sample were carried out under a magnetic field of 0.5 T. The magnetic properties of CoAsSb differ from the diamagnetic behavior observed in CoPn₂. 15 As shown in Figure 5, the value of magnetic susceptibility is positive, which indicates that CoAsSb is not diamagnetic. The field-cooled (FC) and zero-field-cooled (ZFC) curves completely overlap throughout the entire temperature range. The low temperature χ is dominated by a large increase below about 30 K presumably related to impurities. It is also worth noting that there is a pronounced nonlinear shoulder in the low-temperature susceptibility below about 20 K, which suggests interaction effects in the impurity contributions. A small magnetization is observed in the isothermal magnetization curves as a function of field (inset of Figure 5); the sharp decrease of magnetization with increasing temperature corroborates that the low-temperature tail (below ~ 20 K) is due to a small percentage ($\ll 1\%$) of impurities (Figure S4). This behavior suggests that there is no obvious magnetic ordering in CoAsSb and that it is likely to be Pauli paramagnetic. The inverse magnetic susceptibility as a function of temperature (Figure S5) does not obey the Curie-Weiss law.

Thermoelectric Properties above Room Temperature. The electrical resistivity ($\rho_{\rm exp}$) measured from 300 to 1000 K on a dense pellet decreases with increasing temperature

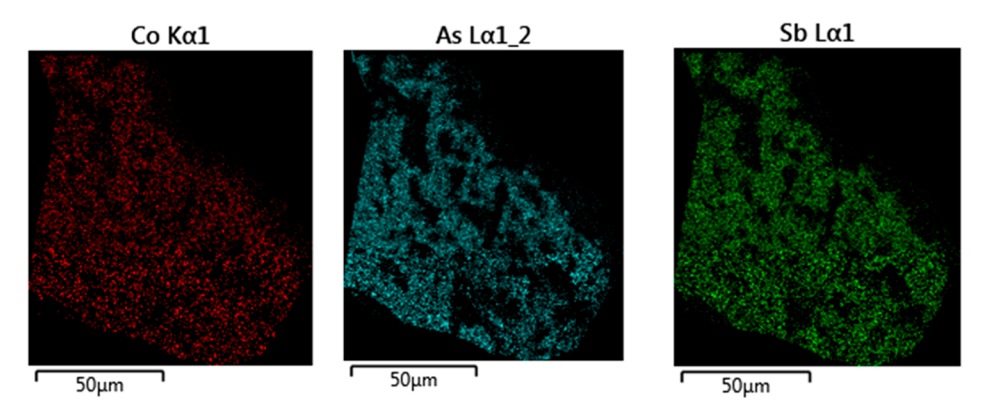


Figure 3. Energy-dispersive X-ray (EDX) mapping of a CoAsSb particle.

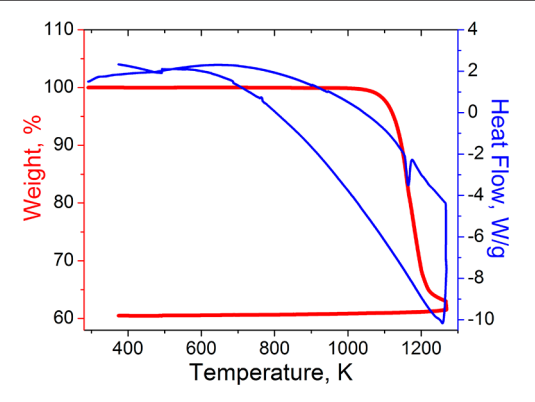


Figure 4. TGA-DSC measurement of CoAsSb between 298 and 1273 K.

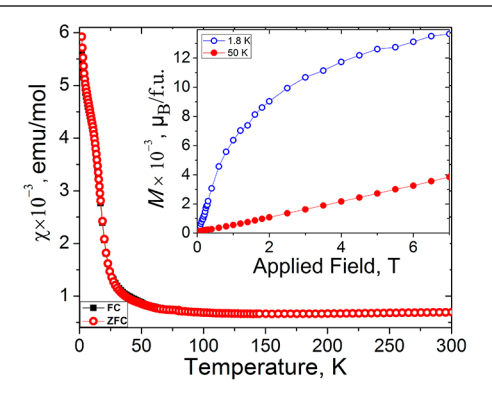


Figure 5. Field-cooled (FC) and zero-field cooled (ZFC) magnetic susceptibilities of CoAsSb as a function of temperature with the applied magnetic field of 0.5 T. Inset shows the magnetization as a function of field measured at 1.8 and 50 K.

(Figure 6). This is typical semiconductor behavior, similar to that of CoAs₂, but unlike that of CoSb₂, which becomes metallic at high temperature. The $\rho_{\rm exp}$ is 7.35 m $\Omega\cdot{\rm cm}$ at 300 K and decreases to 0.72 m $\Omega\cdot{\rm cm}$ at 1000 K; both values are close to borderline metal/semiconductor behavior and suggest a very narrow band gap in CoAsSb. From 300 to 750 K, the $\rho_{\rm exp}$ of CoAsSb is between that of CoAs₂ (50–2 m $\Omega\cdot{\rm cm}$) and CoSb₂ (0.6–1 m $\Omega\cdot{\rm cm}$). For a semiconductor, the thermal activation energy, $E_{\rm av}$ can be calculated from the Arrhenius equation: $\ln \rho = \ln \rho_0 + E_{\rm a}/k_{\rm B}T$, where ρ_0 is the preexponential factor, $k_{\rm B}$ is the Boltzmann constant, and T is the temperature. In the plot of $\ln \rho$ versus of 1/T (K $^{-1}$), two temperature ranges of 975–575 and 475–325 K can be fit linearly, which output $E_{\rm a}$ equal to 0.123(2) and 0.062(1) eV, respectively. The $E_{\rm a}$ is related to the band gap energy $E_{\rm g}$ with $E_{\rm a} \approx E_{\rm g}/2$; hence, the

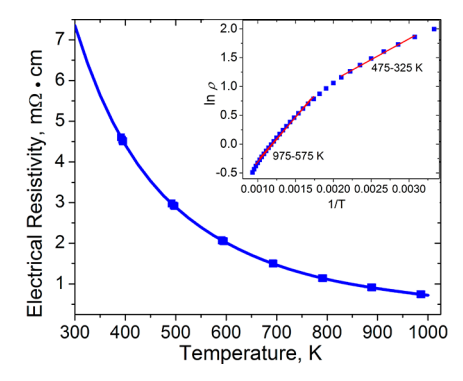


Figure 6. Electrical resistivity as a function of temperature and a plot of $\ln \rho$ (m Ω -cm) vs 1/T (K⁻¹) with linear fitting of the data (inset). The dots are experimental data, and the line is the sixth-order polynomial fit of the data.

corresponding approximate $E_{\rm g}$ are in the range of 0.256(4) and 0.124(4) eV.

The Seebeck coefficient, S_{exp} , is negative from 300 to 1000 K, which indicates that CoAsSb is an n-type semiconductor (Figure 7a). At 300 K, the $S_{\rm exp}$ is $-98~\mu{\rm V/K}$ and increases to a maximum absolute value $(-132 \,\mu\text{V/K})$ at 450 K. Based on this maximum $S_{\rm exp}$ value, the band gap is estimated to be \sim 0.12 eV, which is in reasonable agreement with the range of 0.256(4) and 0.124(4) eV obtained from fitting the resistivity data. The absolute value of $S_{\rm exp}$ decreases with increasing temperature, reaching $-69~\mu\mathrm{V/K}$ at 1000 K. This result is consistent with a previous brief report of CoAsSb, where $S_{\rm exp}$ is $-180~\mu{\rm V/K}$ at room temperature. 36 This value of $S_{\rm exp}$ is also similar to that of $CoAs_2$ (-200, -27 $\mu V/K$), which is also a n-type semiconductor. CoSb₂ was reported to be a p-type semiconductor with a much lower α value (24 $\mu V/K$) and exhibits a transition from p-type to n-type semiconductor.³⁴ The room-temperature carrier concentration of CoAsSb, obtained from the PPMS data is approximately 4.1×10^{19} cm⁻³, and the Hall measurement is consistent with electrons as the dominant carriers. The value of the carrier concentration is between that of CoAs₂ (2.8 × 10^{18} cm^{-3}) and CoSb₂ (1.3 × 10^{20} cm^{-3}). ³⁴ The room temperature electrical conductivity (σ) of CoAsSb was obtained from the Linseis LSR-3 data, and the room temperature mobility (μ), calculated from $\sigma = ne\mu$, was found to be 20.7 cm²/(V s). This μ is much lower than that of CoAs₂ (45.5 cm²/(V s)) and $CoSb_2$ (72.3 cm²/(V s)).³⁴ The carrier concentration is not affected by disorder; therefore, it was expected to fall between the two end compounds. The mobility, however, is affected by disorder; a 50/50 substituted sample will have maximum

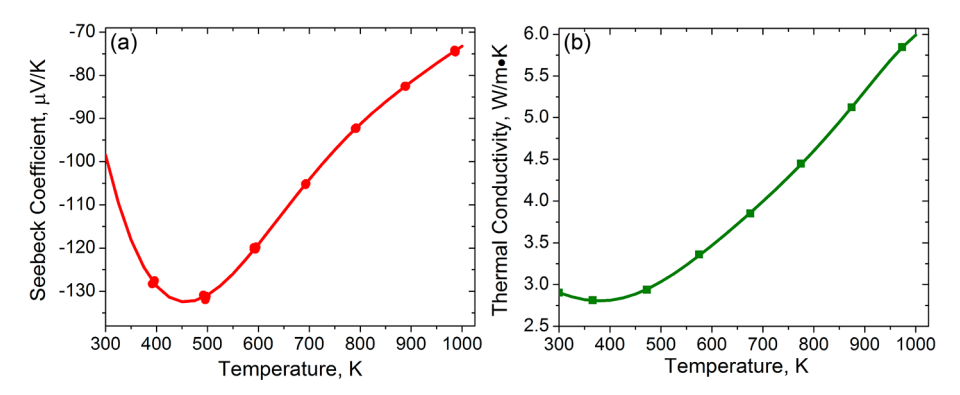


Figure 7. Seebeck coefficient (a) and thermal conductivity (b) of CoAsSb as a function of temperature. The dots are experimental data, and lines are the sixth-order polynomial fitting of the data.

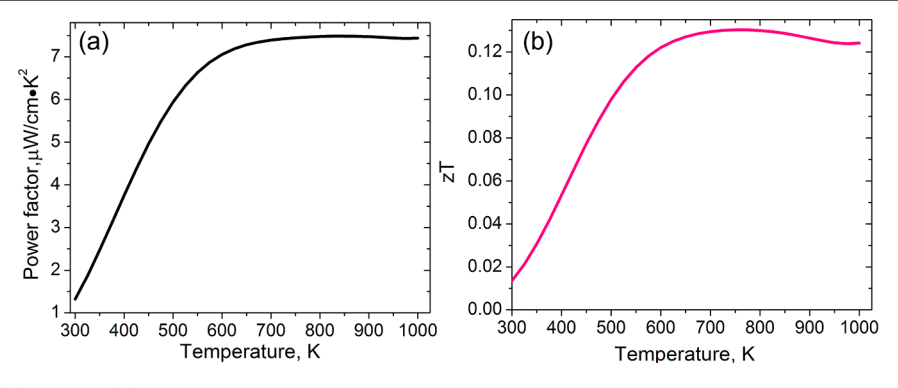


Figure 8. Power factor (a) and zT (b) of CoAsSb as a function of temperature.

configurational disorder, and hence the observed lower mobility of CoAsSb is expected.

The total thermal conductivity, κ_{total} of CoAs₂ and CoSb₂ decreases with increasing temperature in the arsenopyrite phase and then increases at 800 and 644 K, respectively, when the phase transition to marcasite occurs. ^{35,36} However, the κ_{total} of CoAsSb only decreases slightly from 300 to 370 K and then steadily increases with increasing temperature to reach the maximum (6.0 W/(m K)) around 1000 K (Figure 7b). The absence of any obvious slope change in the κ data confirms the absence of any structural transition in CoAsSb.

The total thermal conductivity of CoAsSb, calculated as κ_{total} = $D \times \rho \times C_n$, where the thermal diffusivity (D) is measured as temperature change, density (ρ) is the room temperature value (7.421 g/cm³), and heat capacity ($C_p = 293.42 \text{ J/(kg K)}$) is estimated from the Dulong-Petit law, is between 2.9 and 6.0 W/(m K), which is smaller than those of CoAs₂ (5-12 W/(m K)) and $CoSb_2$ (6–13 W/(m K)). The electronic thermal conductivity, $\kappa_{\rm elec}$ is calculated based on the Wiedemann– Franz equation, $\kappa_{\rm elec} = LT/\rho$, where L is the free Lorentz number, $2.44 \times 10^{-8} \ {\rm W} \cdot {\rm \Omega} \cdot {\rm K}^{-2}$ (Figure S6). The free electron Lorenz value was also used for calculating the κ_{elec} of CoAs₂ and CoSb₂.³⁴ The corresponding lattice thermal conductivity (κ_{lat}) is calculated by subtracting κ_{elec} from κ_{total} (Figure S6). The value of κ_{lat} is between 2.58 and 2.85 W/(m K), much smaller than those of $CoAs_2$ (4-12 W/(m K)) and $CoSb_2$ (4.5-8.5 W/(m K)).³⁴ This is as expected since the formation of a solid solution between similar-type materials decreases phonon scattering via mass fluctuations on different crystallographic sites. In addition, the vacancies on Sb sites in the structure may also contribute to lowering the κ_{lat} . The power factor, PF = S^2/ρ , increases with increasing temperature and remains constant $\approx 7.2 \,\mu\text{W}/(\text{cm K}^2)$

above 550 K and achieves a maximum (7.5 μ W/(cm K²)) at 775 K (Figure 8a). The calculated zT shows a similar trend as the PF below 750 K: with increasing temperature it reaches a maximum, 0.13, at 750 K (Figure 8b). Above 750 K, the zT value slightly decreases to 0.124 at 1000 K. The zT values in the high temperature range are overall higher than that of CoAs₂ (~0.1 at 900 K) or CoSb₂ (~0.05 at 900 K)³⁴ and much higher than that of FeSb₂ (0.005).

Thermoelectric properties including S and κ_{total} were also measured below room temperature (Figure S7a). However, a different measurement setup was used as discussed in the Materials and Methods section. Unlike for FeSb₂, there is no evidence of any abnormal behavior of the *S* at low temperature. The S is also negative below 300 K, and the absolute value increases as the temperature increases, which is in agreement with the trend shown in the high temperature range between 300 and 450 K (Figure 7a). Similar to the κ_{total} observed above room temperature, the κ_{total} measured below room temperature increases as a function of increasing temperature (Figure S7b). The data above 250 °C is attributed to the emissivity of the sample at high temperatures. 45 The maximum value is 1.9 W/(m K) at 300 K, which is close to the value measured in the high temperature range. At low temperature, the ρ was not recorded accurately by a two-probe method; the data therefore is not presented here.

Theoretical Calculations. From local density approximations (LDA), CoAsSb is a semimetal with a clear dip at the Fermi level in the density of states. The density of states around the dip is mostly contributed by the Co states (Figure 9b). Two bands of mainly Co d-character cross the Fermi level, resulting in two small Fermi pockets: one of electron-type is centered at the Y point, and the other of hole-type is near to both the

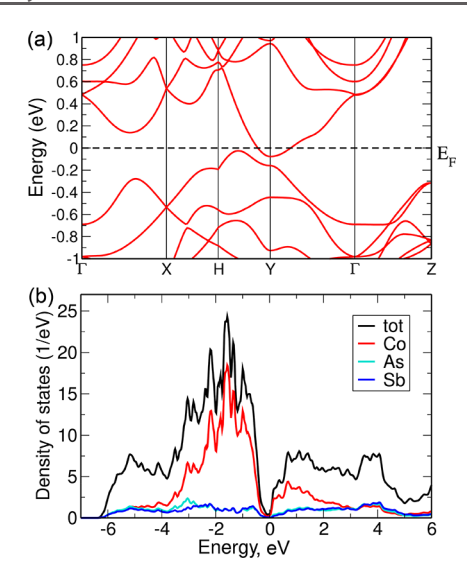


Figure 9. Electronic band structure and density of states plots for CoAsSb calculated with LDA.

H and Y points, but not crossing the H-Y line as shown in the band structure (Figure 9a). LDA calculations indicate that there is a direct band gap around 80 meV between these two bands at the Y point.

The calculated semimetal is different from the semiconductor observed in the electric resistivity experiment. However, calculation is carried out on stoichiometric CoAsSb without considering Sb vacancies, while the measurement is carried out on CoAsSb_{0.883}. The observed semiconducting behavior may be due to the disordered Sb vacancies. The theoretical calculation using LDA here serves as a rough guidance and underestimates the band gap in CoAsSb that leads to semimetallic behavior. However, with a more advanced DFT calculation, the mBJ exchange potential method, a band gap of 0.074 eV is

obtained (Figure S8), which is consistent with the band gap of 0.12–0.25 eV based on the electrical resistivity data. It is worth noting that the band gap is only obtained with the DFT relaxed structure with the lattice parameters, a = 6.22918, b = 6.14171, c = 6.26213 Å, and $\beta = 116.17^{\circ}$ (i.e., relative to the refined experimental data: a = 6.23704(6), b = 6.13276(4), c = 6.21963(6) Å, and $\beta = 116.6396(4)^{\circ}$).

The electrical resistivity was calculated ($\rho_{\rm calc}$) by choosing a relaxation time, 3.6×10^{-15} , to match the experimental value around 800 K (Figure 10a). The $\rho_{\rm calc}$ decreases as the temperature increases, which is similar to the experimental data, but with a more gradual slope. Thus, $\rho_{\rm calc}$ is smaller than $\rho_{\rm exp}$ below 800 K. The computed Seebeck coefficient ($S_{\rm calc}$) has a negative sign in the measured temperature range, with a maximum value as large as about $-87~\mu V/{\rm K}$, not far from the $S_{\rm exp}$ of $-130~\mu V/{\rm K}$ (Figure 10b). However, this maximum appears at higher temperature in the calculation than in the measurements. The $S_{\rm calc}$ agrees better with $S_{\rm exp}$ in the high temperature region, above 800 K. The difference between $S_{\rm calc}$ and $S_{\rm exp}$ may be due to the nonstoichiometry of the Sb content, which is not considered in the theoretical calculation.

Based on the values of $\rho_{\rm calc}$ and $S_{\rm calc}$, the PF can be plotted as shown in Figure 10c. Between 300 and 1000 K, the PF increases almost linearly with increasing temperature and reaches the maximum value of 8.2 μ W/(cm K²), close to the experimental value (7.2 μ W/(cm K²)). The $\kappa_{\rm elec}$ was also calculated with the BoltzTrap package (Figure S9), and it shows a similar trend as the experimental $\kappa_{\rm total}$ and the calculated value of $\kappa_{\rm elec}$ is somewhat larger than the experimentally determined $\kappa_{\rm total}$. Using the calculated $\kappa_{\rm elec}$ as the calculated $\kappa_{\rm total}$ one can estimate the zT, which increases with increasing temperature and reaches a maximum (0.118) above 850 K and which agrees well with the experimental value of 0.12. When $\kappa_{\rm lat}$ (not calculated here) is also considered in the calculation, then the estimated zT value is expected to be much smaller than the experimental value.

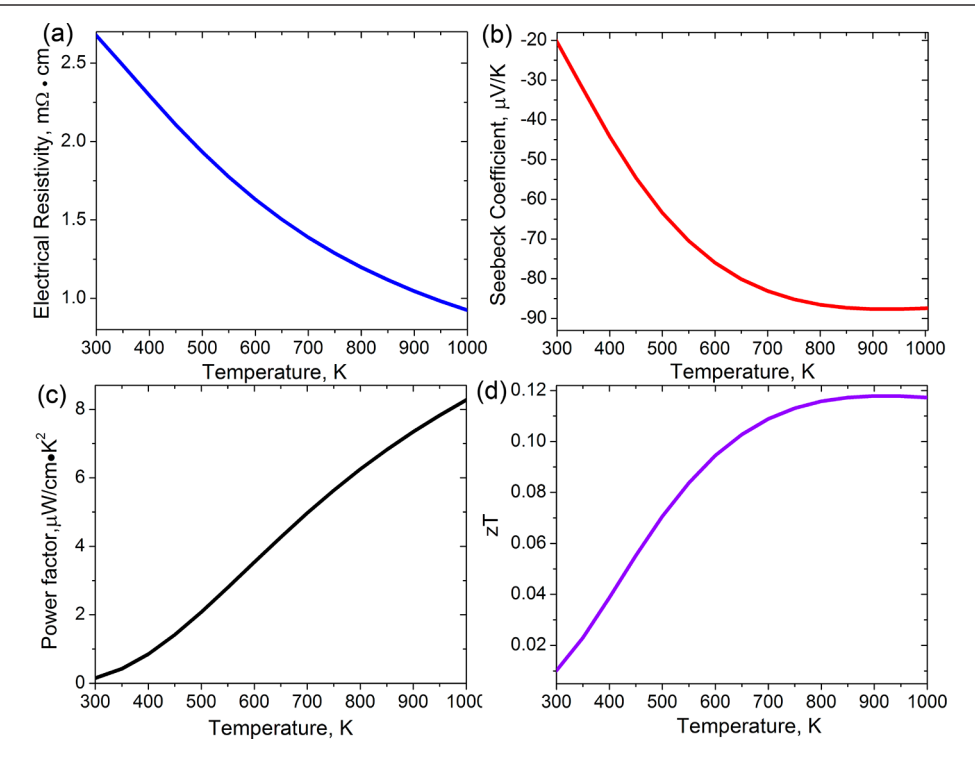


Figure 10. Calculated resistivity (a), Seebeck coefficient (b), powder factor (c), and zT (d) values as a function of temperature.

The overestimated κ_{elec} and underestimated zT are likely due to the underestimation of the band gap by LDA.

To estimate the effect of Sb site vacancy on the electronic structure and transport properties, the LDA rigid band approximation method was used. For the CoAsSb_{0.883} composition, the Sb deficiency shifts the Fermi level $(E_{\rm F})$ 0.924 eV to lower energy (Figure S10). In comparison with the transport properties of CoAsSb, the $\sigma_{\rm calc}$ of CoAsSb $_{0.883}$ increases (Figure S11). This is reasonable because the density of states at the Fermi level increases; the carrier concentration probably also increases. The S_{calc} still shows the feature of an n-type semiconductor, but with a smaller value, which results in a smaller overall power factor. The calculated $\kappa_{\rm elec}$ increases, and the lattice thermal conductivity κ_{lat} most likely will decrease. The estimated κ_{lat} is not available because it is complicated and time-consuming to achieve a reliable calculated κ_{lat} . Therefore, it is difficult to predict how the zT value changes due to Sb vacancies. An experimental study of Sb deficiency on FeSb2 shows a positive effect; thus, one may speculate that Sb deficiency will improve the thermoelectric properties of CoAsSb as well.46 In addition, the transport properties as a function of chemical potential near the $E_{\rm F}$ of CoAsSb at 300 K is calculated (Figure S12). The conductivity increases when $E_{\rm F}$ shifts to either lower or higher energy. The largest S and power factor are obtained when $E_{\rm F}$ is shifted about 0.1 eV to higher energy (Figure S12b,c). The $\kappa_{\rm elec}$ is not increased much within the range of 0.1 eV (Figure S12d); hence, the thermoelectric properties of CoAsSb at 300 K can be improved by proper electron doping.

Overall, the presented LDA calculations provide a good starting point for further understanding and engineering the thermal properties in CoAsSb and related materials. Further investigations with advanced techniques beyond LDA would improve quantitative agreement between theory and experiment.

CONCLUSIONS

Polycrystalline CoAsSb was successfully synthesized at ambient pressure at a relatively mild temperature of 1073 K. Structural analysis with SPXD indicates that it adopts an arsenopyritetype structure instead of marcasite-type. Structural transition from arsenopyrite-type to marcasite at high temperature was not observed, which is different from the cases of CoPn₂ (Pn = As, Sb). CoAsSb exhibits semiconducting electrical transport with a very narrow band gap, much smaller than those of CoPn₂. The S_{exp} reaches a maximum of $-132.42 \,\mu\text{V/K}$ at 450 K, similar to that of CoAs₂ (-200, -27 μ V/K), which is also an n-type semiconductor. Because of the smaller κ_{total} than those of CoPn2, CoAsSb exhibits a higher zT value, with a maximum of 0.13 at 750 K. First-principles calculations were performed to elucidate the electronic structure. Many aspects of the measured transport properties are captured by a simple Boltzmann transport picture, and the deviations indicate that the band gap is likely underestimated in the calculations. The overall estimated zT value based on calculated $\kappa_{\rm elec}$ $\rho_{\rm calc}$ and $S_{\rm calc}$ is in agreement with the experimental value in the high temperature range above 800 K. Theoretical studies of the effect of Sb vacancies on the transport properties indicate a larger $\kappa_{\rm elec}$, smaller $S_{\rm calc}$ and smaller PF. The thermoelectric performance of CoAsSb could be improved by proper electron doping.

Compared to FeSb₂, the Seebeck coefficient and power factor of CoAsSb are much smaller, but the zT value of CoAsSb is significantly larger than that of FeSb₂ (zT = 0.005 at 12 K). As demonstrated in this work, CoAsSb has a smaller κ compared to that of CoPn₂. Therefore, we expect that FeAsSb will

show similar behavior and will also have a smaller κ than that of FeSb₂ and, hence, greatly improved thermoelectric properties than FeSb₂. Our recent calculations also support this speculation and indicate that FeAsSb may form at high pressure. ⁴⁷ The synthesis of FeAsSb at high pressure is ongoing, and the results will be reported in due course.

ASSOCIATED CONTENT

S Supporting Information

The Supporting Information is available free of charge on the ACS Publications website at DOI: 10.1021/acs.chemmater.7b05170.

Powder X-ray pattern compared with calculated arsenopyrite and marcasite structure types; summary of Rietveld refinement of CoAsSb synchrotron powder X-ray pattern; SEM image of CoAsSb particles; X-ray diffraction pattern of samples before and after TGA measurement; the fitting of magnetization as a function of field of CoAsSb measured at 1.8 and 50 K; the inverse magnetic susceptibility of CoAsSb; electronic and lattice thermal conductivities of CoAsSb; Seebeck coefficient and thermal conductivity of CoAsSb below room temperature; electronic band structure and DOS for CoAsSb with DFT relaxation calculation; the calculated electronic thermal conductivity of CoAsSb with the BoltzTrap package; DOS of CoAsSb_{0.883} with LDA rigid band approximation method; transport properties of CoAsSb_{0.883}; and transport properties as a function of chemical potential near the Fermi level of CoAsSb at 300 K (PDF)

AUTHOR INFORMATION

Corresponding Authors

*E-mail: greenbla@chem.rutgers.edu (M.G.). *E-mail: kotliar@physics.rutgers.edu (G.K.).

ORCID (

Xiaoyan Tan: 0000-0002-1742-8252

Susan M. Kauzlarich: 0000-0002-3627-237X Martha Greenblatt: 0000-0002-1806-2766

Notes

The authors declare no competing financial interest.

ACKNOWLEDGMENTS

M.G., G.K., and X.T. were supported by the Center for Computational Design of functional Strongly Correlated Materials and Theoretical Spectroscopy under DOE Grant DE-FOA-0001276. S.M.K. and K.P.D. thank NSF DMR-1709382 for funding. Use of the Advanced Photon Source at Argonne National Laboratory was supported by the U.S. Department of Energy, Office of Science, Office of Basic Energy Sciences, under Contract DE-AC02-06CH11357. Chang Jong Kang was supported by NSF grant DMR-1733071.

REFERENCES

- (1) Jain, A.; Shin, Y.; Persson, K. A. Computational Predictions of Energy Materials Using Density Functional Theory. *Nat. Rev. Mater.* **2016**, *1*, 15004.
- (2) Hautier, G.; Jain, A.; Ong, S. P. From Computer to the Laboratory: Materials Discovery and Design Using First-Principles Calculations. *J. Mater. Sci.* **2012**, *47*, 7317–7340.
- (3) Chen, W.; Pöhls, J. H.; Hautier, G.; Broberg, D.; Bajaj, S.; Aydemir, U.; Gibbs, Z. M.; Zhu, H.; Asta, M.; Snyder, G. J.; Meredig, B.; White, M. A.; Persson, K.; Jain, A. Y. Understanding Thermoelectric Properties from High-Throughput Calculations: Trends,

Insights, and Comparisons with Experiment. J. Mater. Chem. C 2016, 4, 4414–4426.

- (4) Meredig, B.; Agrawal, A.; Kirklin, S.; Saal, J.; Doak, J.; Thompson, A.; Zhang, K.; Choudhary, A.; Wolverton, C. Combinatorial Screening for New Materials in Unconstrained Composition Space with Machine Learning. *Phys. Rev. B: Condens. Matter Mater. Phys.* **2014**, 89, 094104.
- (5) Meredig, B.; Wolverton, C. Dissolving the Periodic Table in Cubic Zirconia; Data Mining to Discover Chemical Trends. *Chem. Mater.* **2014**, 26, 1985–1991.
- (6) Gaultois, M. W.; Oliynyk, A. O.; Mar, A.; Sparks, T. D.; Mulholland, G. J.; Meredig, B. Perspective: Web Based Machine Learning Models for Real-Time Screening of Thermoelectric Materials Properties. *APL Mater.* **2016**, *4*, 053213.
- (7) Caillat, T. Preparation and Thermoelectric Properties of Some Arsenopyrite Phases Based on RuSb_{2-2x}Te_{2x} and RuSb_{2-2x}Se_{2x} Solid Solutions. *J. Phys. Chem. Solids* **1998**, *59*, 61–67.
- (8) Sales, B. C.; May, A. F.; McGuire, M. A.; Stone, M. B.; Singh, D. J.; Mandrus, D. Transport, Thermal, and Magnetic Properties of the Narrow-Gap Semiconductor CrSb₂. *Phys. Rev. B: Condens. Matter Mater. Phys.* **2012**, *86*, 235136.
- (9) Bugaris, D. E.; Malliakas, C. D.; Shoemaker, D. P.; Do, D. T.; Chung, D. Y.; Mahanti, S. D.; Kanatzidis, M. G. Crystal Growth and Characterization of the Narrow-Band-Gap Semiconductors OsPn₂ (Pn = P, As, Sb). *Inorg. Chem.* **2014**, *53*, 9959–9968.
- (10) Li, G.; Bajaj, S.; Aydemir, U.; Hao, S.; Xiao, H.; Goddard, W. A., III; Zhai, P.; Zhang, Q.; Snyder, G. J. p-Type Co Interstitial Defects in Thermoelectric Skutterudite CoSb₃ Due to the Breakage of Sb₄-Rings. *Chem. Mater.* **2016**, 28, 2172–2179.
- (11) Gonçalves, A. P.; Godart, C. New Promising Bulk Thermoelectrics; Intermetallics, Pnictides, and Chalcogenides. *Eur. Phys. J. B* **2014**, 87, 42.
- (12) Petrovic, C.; Kim, J. W.; Bud'ko, S. L.; Goldman, A. I.; Canfield, P. C.; Choe, W.; Miller, G. J. Anisotropy and Large Magnetoresistance in the Narrow-Gap Semiconductor FeSb₂. *Phys. Rev. B: Condens. Matter Mater. Phys.* **2003**, *67*, 155205.
- (13) Bentien, A.; Johnsen, S.; Madsen, G. K. H.; Iversen, B. B.; Steglich, F. Colossal Seebeck Coefficient in Strongly Correlated Semiconductor FeSb₂. *Europhys. Lett.* **2007**, *80*, 17008.
- (14) Sun, P.; Oeschler, N.; Johnsen, S.; Iversen, B. B.; Steglich, F. Huge Thermoelectric Power Factor: FeSb₂ versus FeAs₂ and RuSb₂. Appl. Phys. Express **2009**, 2, 091102.
- (15) Tomczak, J. M.; Haule, K.; Miyake, T.; Georges, A.; Kotliar, G. Thermopower of Correlated Semiconductors: Application to FeAs₂ and FeSb₂. *Phys. Rev. B: Condens. Matter Mater. Phys.* **2010**, 82, 085104.
- (16) Diakhate, M. S.; Hermann, R. P.; Möchel, A.; Sergueev, I.; Søndergaard, M.; Christensen, M.; Verstraete, M. J. Thermodynamic, Thermoelectric, and Magnetic Properties of FeSb₂: A Combined First-principles and Experimental Study. *Phys. Rev. B: Condens. Matter Mater. Phys.* **2011**, *84*, 125210.
- (17) Jie, Q.; Hu, R.; Bozin, E.; Llobet, A.; Zaliznyak, I.; Petrovic, C.; Li, Q. Electronic Thermoelectric Power Factor and Metal-Insulator Transition in FeSb₂. *Phys. Rev. B: Condens. Matter Mater. Phys.* **2012**, 86, 115121.
- (18) Battiato, M.; Tomczak, J. M.; Zhong, Z.; Held, K. Unified Picture for the Colossal Thermopower Compound FeSb₂. *Phys. Rev. Lett.* **2015**, *114*, 236603.
- (19) Saleemi, M.; Tafti, M. Y.; Jacquot, A.; Jägle, M.; Johnsson, M.; Toprak, M. S. Chemical Synthesis of Iron Antimonide (FeSb₂) and Its Thermoelectric Properties. *Inorg. Chem.* **2016**, *55*, 1831–1836.
- (20) Takahashi, H.; Okazaki, R.; Ishiwata, S.; Taniguchi, H.; Okutani, A.; Hagiwara, M.; Terasaki, I. Colossal Seebeck Effect Enhanced by Quasi-ballistic Phonons Dragging Massive Electrons in FeSb₂. *Nat. Commun.* **2016**, *7*, 12732.
- (21) Hulliger, F.; Mooser, E. Semiconductivity in Pyrite, Marcasite and Arsenopyrite Phase. *J. Phys. Chem. Solids* **1965**, *26*, 429–433.

- (22) Holseth, H.; Kjekshus, A.; Andresen, A. F.; Pearson, W. B. Compounds with the Marcasite Type Crystal Structure. *Acta Chem. Scand.* **1968**, 22, 3273–3283.
- (23) Fan, K. L.; Rosenthal, G. H.; Mckinzie, H. L.; Wold, A. Preparation and Properties of FeAs₂ and FeSb₂. *J. Solid State Chem.* **1972**, *5*, 136–143.
- (24) Bentien, A.; Madsen, G. K. H.; Johnsen, S.; Iversen, B. B. Experimental and Theoretical Investigations of Strongly Correlated FeSb_{2-x}Sn_x. *Phys. Rev. B: Condens. Matter Mater. Phys.* **2006**, 74, 205105.
- (25) Hu, R.; Mitrović, V. F.; Petrovic, C. Anisotropy in the Magnetic and Transport Properties of Fe_{1-x}Co_xSb₂. *Phys. Rev. B: Condens. Matter Mater. Phys.* **2006**, 74, 195130.
- (26) Hu, R.; Hermann, R. P.; Grandjean, F.; Lee, Y.; Warren, J. B.; Mitrović, V. F.; Petrovic, C. Weak Ferromagnetism in $Fe_{1-x}Co_xSb_2$. *Phys. Rev. B: Condens. Matter Mater. Phys.* **2007**, *76*, 224422.
- (27) Hu, R.; Mitrović, V. F.; Petrovic, C. Anisotropy in the Magnetic and Electrical Transport Properties of Fe_{1-x}Cr_xSb₂. *Phys. Rev. B: Condens. Matter Mater. Phys.* **2007**, *76*, 115105.
- (28) Sun, P.; Oeschler, N.; Johnsen, S.; Iversen, B. B.; Steglich, F. Narrow Band Gap and Enhanced Thermoelectricity in FeSb₂. *Dalton Trans.* **2010**, *39*, 1012–1019.
- (29) Sun, P.; Søndergaard, M.; Sun, Y.; Johnsen, S.; Iversen, B. B.; Steglich, F. Unchanged Thermopower Enhancement at the Semi-conductor-Metal Transition in Correlated FeSb_{2-x}Te_x. *Appl. Phys. Lett.* **2011**, *98*, 072105.
- (30) Wang, K.; Hu, R.; Warren, J.; Petrovic, C. Enhancement of the Thermoelectric Properties in Doped FeSb₂ Bulk Crystals. *J. Appl. Phys.* **2012**, *112*, 013703.
- (31) Fuccillo, M. K.; Gibson, Q. D.; Ali, M. N.; Schoop, L. M.; Cava, R. J. Correlated Evolution of Colossal Thermoelectric Effect and Kondo Insulating Behavior. *APL Mater.* **2013**, *1*, 062102.
- (32) Quesnel, J. C.; Heyding, R. D. Transition Metal Arsenides V. A Note on the Rhodium/Arsenic System and the Monoclinic Diarsenides of the Cobalt Family. *Can. J. Chem.* **1962**, *40*, 814–818.
- (33) Kjekshus, A.; et al. On the Properties of Binary Compounds with the CoSb₂ Type Crystal Structure. *Acta Chem. Scand.* **1971**, 25, 411–422.
- (34) Goto, Y.; Miyao, S.; Kamihara, Y.; Matoba, M. Electrical/ Thermal Transport and Electronic Structure of the Binary Cobalt Pnictides CoPn₂ (Pn = As and Sb). *AIP Adv.* **2015**, *5*, 067147.
- (35) Kjekshus, A.; Rakke, T. High Temperature Studies of Marcasite and Arsenopyrite Type Compounds. *Acta Chem. Scand. A* **1977**, *31*, 517–529.
- (36) Siegrist, T.; Hulliger, F. High-Temperature Behavior of CoAs₂ and CoSb₂. *J. Solid State Chem.* **1986**, *63*, 23–30.
- (37) Dobbe, R. T. M.; Zakrzewski, M. A. Oenite, CoSbAs, A New Mineral Species from the Tunaberg Cu-Co-Sulfide Skarns, Bergslagen, Sweden. *Can. Mineral.* **1998**, *36*, 855–860.
- (38) Rodríguez-Carvajal, J. Recent Advances in Magnetic-Structure Determination by Neutron Powder Diffraction. *Phys. B* **1993**, *192*, 55–69.
- (39) Blaha, P.; Schwarz, K.; Madsen, G. K. H.; Kvasnicka, D.; Luitz, J. WIEN2K, An Augmented Plane Wave + Local Orbitals Program for Calculating Crystal Properties; Schwarz, K., Ed.; Technische Universität Wien: Wien, Austria, 2001.
- (40) Madsen, G. K. H.; Singh, D. J. BoltzTraP. A Code for Calculating Band-structure Dependent Quantities. *Comput. Phys. Commun.* **2006**, 175, 67–71.
- (41) Tran, F.; Blaha, P. Accurate Band Gaps of Semiconductors and Insulators with a Semilocal Exchange-Correlation Potential. *Phys. Rev. Lett.* **2009**, *102*, 226401.
- (42) Kjekshus, A.; et al. On the Properties of Binary Compounds with the CoSb₂ Type Crystal Structure. *Acta Chem. Scand.* **1971**, 25, 411–422.
- (43) Schicketanz, H.; Terzieff, P. Lattice Parameter and Electronic Properties of the Solid Solution CoSb₂-CoTe₂. *J. Alloys Compd.* **1996**, 232, 26–31.

(44) Goldsmid, H. J.; Sharp, J. W. Estimation of the Thermal Band Gap of a Semiconductor from Seebeck Measurements. *J. Electron. Mater.* **1999**, 28, 869–872.

- (45) Wang, J.; Lebedev, O. I.; Lee, K.; Dolyniuk, J.; Klavins, P.; Bux, S.; Kovnir, K. High-efficiency Thermoelectric Ba₈Cu₁₄Ge₆P₂₆ Bridging the Gap between Tetrel-based and Tetrel-free Clathrates. *Chem. Sci.* **2017**, *8*, 8030–8038.
- (46) Sanchela, A. V.; Thakur, A. D.; Tomy, C. V. Enhancement in Thermoelectric Properties of FeSb₂ by Sb Site Deficiency. *J. Materiomics* **2015**, *1*, 205–212.
- (47) Kang, C.-J.; Kotliar, G. Study for Material Analogs of FeSb₂: Material Design for Thermoelectric Materials. *Phys. Rev. Materials* **2018**, *2*, 034604.